

# The conundrum of functional brain networks: small-world or fractal modularity

Lazaros K. Gallos<sup>1</sup>, Hernán A. Makse<sup>2</sup>, Mariano Sigman<sup>2</sup>

<sup>1</sup> *Levich Institute and Physics Department,*

*City College of New York, New York, New York 10031, USA*

<sup>2</sup> *Integrative Neuroscience Laboratory, Physics Department,*

*FCEyN, Universidad de Buenos Aires, Buenos Aires, Argentina*

(Dated: January 8, 2019)

## Abstract

The human brain is organized in functional modules. Such an organization poses a conundrum: modules ought to be sufficiently independent to guarantee functional specialization and sufficiently connected to bind multiple processors for efficient information transfer. It is commonly accepted that small-world architecture may solve this problem. However, there is intrinsic tension between shortcuts generating small-worlds and the persistence of modules. Here we provide a solution to this puzzle. We show that the functional brain network formed by percolation of strong links is highly modular. Contrary to the common view, modules are self-similar and therefore are very far from being small-world. Incorporating the weak ties to the network converts it into a small-world preserving an underlying backbone of well-defined modules. Weak ties are organized precisely as predicted by theory maximizing information transfer with minimal wiring costs. This trade-off architecture is reminiscent of the “strength of weak ties” crucial concept of social networks and provides a natural solution to the puzzle of efficient information flow in the highly modular structure of the brain.

One of the main findings in neuroscience is the modular organization of the brain which in turn implies the parallel nature of brain computations [1]. For example, in the visual modality, more than thirty visual areas analyze simultaneously distinct features of the visual scene: motion, color, orientation, space, form, luminance and contrast among others [2]. These features, as well as information from different sensory modalities, have to be integrated, as one of the main aspects of perception is its unitary nature [1, 3].

This leads to a basic conundrum of brain networks: modular processors have to be sufficiently isolated to achieve independent computations, but also globally connected to be integrated in coherent functions [4]. A widely accepted view is that small-world networks confer a capability for both specialized processing and integrated processing over the entire network since they combine high local clustering and short path length [5–7]. This view has been fueled by the systematic finding of small-world topology in a wide range of human brain networks derived from functional [8–10], structural [11] and diffusion tensor [12] MRI. Small-world topology has also been identified at the cellular-network scale in functional cortical neuronal circuits in mammals [13, 14] and even in the nervous system of the nematode *Caenorhabditis Elegans* [6], so far the only one to be comprehensively mapped at a cellular level. Moreover, small-world property seems to be relevant for brain function since it is affected by disease [15], with normal aging and by pharmacological blockade of dopamine neurotransmission [9].

Despite this common belief, and systematic experimental observations, traditional models of small-world networks cannot fully capture the coexistence of highly modular structure with broad global integration. Local clustering and modularity are independent network features. The clustering coefficient, the typical measure of clustering, is a purely local quantity which can be assessed inspecting the immediate neighborhood of a node. On the contrary, modularity is a global property of the network, determined by the existence of strongly connected groups of nodes that are only loosely connected to the rest of the network. In principle, modularity cannot be inferred from local clustering and vice versa. In fact, it is easy to construct modular and unclustered networks or, reciprocally, clustered networks without modules. More importantly, small world-topology is typically incompatible with strong modularity [16]. While a clustered network preserves its clustering when a small fraction of shortcuts are added (converting it into a small-world) [6], the persistence of modules is not equally robust, and the shrinking of the network diameter may quickly

destroy the modules.

Hence, the concept of a small-world network is not adequate by itself to explain the modular and integration features of brain networks on its own. We propose that a solution to modularity and broad integration can be achieved by a network comprised by two different layers: a layer formed by strong links with a highly modular, non small-world topology and an underlying network of weak ties which establish shortcuts between modules converting it to a non-structured (non-modular) small-world network. At low connectivity thresholds, when the network is fully connected, weak connections confer small-world properties in agreement with most previous observations.

This proposal is inspired by a fundamental notion of sociology termed “the strength of weak ties” [17, 18]: according to this theory, strong ties (close friends) clump together forming modules. An acquaintance (weak tie) becomes a crucial bridge (a shortcut) between the two densely knit clumps (modules) of close friends [17].

Interestingly, this idea emerges also in neuronal circuits [13] where stronger connections tend to be more clustered than weaker ones, a structure referred to as a skeleton of stronger connections in a sea of weaker ones. This theme also emerges in theoretical models of large-scale cognitive architecture. Integration of information across modules is referred as the binding problem in psychology [3]. Several theories have suggested mechanisms based on dynamic binding [4, 19] or on a workspace system [1, 20]. For instance, the workspace model [1, 20] proposes that a flexible routing system with dynamic and comparably weaker connections transiently connects modules with very strong connections carved by long-term learning mechanisms.

Here we set out to investigate whether in effect, brain networks conform to a two layer structure determined by scale and strength of connections.

**Network analysis.**— We capitalize on a well-known dual-task paradigm, the psychological refractory period [21] in which stimuli from different sensory modalities (visual and auditory) have to be routed to different motor effectors (in our experiment the motor effectors are the left and right hand, see Section I). The temporal gap between the auditory and visual stimuli varied in four different conditions of 0, 300, 900 and 1200 ms. A total of 16 subjects had to respond with the right hand to the visual stimulus and with the left hand to the auditory stimulus. The sequence of activated regions which unfolds during the execution of the task has been reported in a previous manuscript [22]. Here we investigate

how this broad activated region organizes in a network which may achieve modularity and compactness.

Our network analysis relies on time-resolved fMRI based on the phase signal [22]. We first compute the phase of the BOLD-fMRI response on each trial, each subject, and each voxel [22]. We then determine the correlation matrix  $0 \leq c_{ij} \leq 1$  between the  $i$ -th and  $j$ -th voxel measuring the phase correlation between the corresponding pair of voxels for each individual subject and condition (see Section II). Here we do not explore the differences in networks between different conditions. Rather, we consider them as independent experiments, generating a total of 64 different networks, one for each condition of temporal gap and subject.

The connectivity between voxels can be naturally mapped to a percolation problem defined in the  $N \times N$  space of interactions  $c_{ij}$  [23]. We consider each voxel (comprising a volume of  $1 \text{ mm}^3$ ) as a node in the network. A link or tie between nodes  $i$  and  $j$  exists if  $c_{ij} > p$  for a given threshold  $p$  (see Section III).

In general, the size of the largest component of connected links in a percolation process remains very small for small  $p$  and increases abruptly through a critical phase transition at  $p_c$ , in which a single largest connected component spans the whole system [23]. A single incipient connected component of nodes is expected to appear if the links in the network are occupied at random without correlations, i.e. when the probability to find an active bond is uncorrelated with the activity of all the other bonds in the network. When this percolation analysis is applied to the functional brain network a more complex picture emerges revealing non-trivial correlations in brain activity.

For each participant, we calculate the size of the largest connected component as we lower the percolation threshold from  $p = 1$  to 0. We find that, for all participants and stimuli in this study, the size of the largest connected component increases progressively with a series of sharp jumps (Fig. 1A). This is indicative of a multiplicity of percolating components which subsequently merge as  $p$  decreases rather than a single spanning component emerging at a single critical  $p$  as expected for uncorrelated percolation. Each of these jumps define a single percolation transition focused on groups of voxels which are highly correlated, constituting a well-defined module, as shown in Fig. 1B for a typical individual.

Therefore, to identify the modules, we locate the percolation threshold around the first jump in the size of the largest connected component when  $p$  is lowered from  $p = 1$  towards

$p = 0$  that yields three modules of at least 1,000 voxels each ( $p_c = 0.979$  in the example of Fig. 1B). This process results in a total of 192 modules among all participants and stimuli which are pooled together for the present analysis. An example of a module in the network space is shown in the right panel of Fig. 1B, while the left panel in Fig. 1B shows the same module in real space. The topography of these modules reflects coherent patterns across different subjects as shown in Section V.

**Scaling and modular organization.**— To determine the structure of the modules we investigate scaling properties of the mass of each module (the total number of voxels,  $N_c$ ) as a function of three length scales: (i) the maximum network diameter,  $\ell_{\max}$ , (ii) the average network distance between two nodes,  $\langle \ell \rangle$ , and (iii) the maximum Euclidean distance between two nodes of the module,  $r_{\max}$  that are directly connected. The distance in the network space or chemical distance,  $\ell$ , is defined as the number of links along the shortest path between two nodes in the module. The maximum network diameter is the largest shortest path in the network representation.

Figure 2 (central panel) indicates power-law scaling for these quantities defining the fractal dimension of the modules [23]. For instance:

$$N_c(r_{\max}) \sim (r_{\max})^{d_f}, \quad (1)$$

defines the Euclidean Hausdorff fractal dimension,  $d_f = 2.1 \pm 0.2$ . The scaling with  $\ell_{\max}$  and  $\langle \ell \rangle$  is consistent with Eq. (1) as seen in Fig. 2. The fractal dimension  $d_f$  quantifies how densely the area is covered by a specific module.

Equation (1) indicates that all modules, taken globally have a self-similar structure. We next investigate whether the internal structure of each module is also scale-invariant. This can be investigated applying renormalization group (RG) analysis for complex networks [16, 24, 25]. This technique allows one to observe the network at different scales transforming it into successively simpler copies of itself, which can be used to detect characteristics which are difficult to identify at a specific scale of observation [24]. Here we use this technique to characterize sub-modular structure within each module obtained from percolation analysis.

Each module identified by percolation is first tiled with the minimum possible number of boxes or sub-modules,  $N_B$ , of a given chemical distance  $\ell_B$ . The requirement that the number of boxes should be minimized poses an optimization problem which can be solved using the box-covering algorithm explained in [26] (see Section IV and Fig. 3A

explaining the Maximum Excluded Mass Burning algorithm, MEMB, downloaded from [http://lev.ccny.cuny.edu/~hmakse/soft\\_data.html](http://lev.ccny.cuny.edu/~hmakse/soft_data.html)). The resulting boxes are characterized by the proximity between all their nodes and minimization of the links outside the boxes. Thus, the box-covering algorithm detects boxes/submodules that also tend to maximize modularity.

Different values of the box diameter  $\ell_B$  yield a different partition of the percolation modules in submodules of varying sizes (Fig. 3A). The right panel in Fig. 2 shows in different colors the identified submodules of size  $\ell_B = 4$  in a typical percolation module. We apply the box-covering algorithm to perform a RG analysis to each of the percolation modules. Figure 3B shows the scaling of  $N_B$  versus  $\ell_B$  averaged over all the modules for all individuals and stimuli. This property is quantified in the power-law relation:

$$N_B(\ell_B) \sim \ell_B^{-d_B}, \quad (2)$$

where  $d_B$  is the box fractal dimension [16, 24, 25]. The exponent  $d_B$  characterizes the self-similarity between different parts of the module. Finite and small values of  $d_B$  show that the network has fractal features in the topological space, where the covering boxes retain their connectivity scheme under different scales, and smaller-scale boxes behave in a similar way as the original network. The resulting  $d_B$  averaged over all the modules is  $d_B = 1.9 \pm 0.1$ . This relatively small value means that the modules are not very dense, resembling more a tree-like structure, enriched with small-scale features such as loops and dangling ends, while at large-scale it presents a more linear form. Combining both results, we find that globally the ensemble of brain modules forms a self-similar structure characterized by Eq. (1). Locally, each module is in turn hierarchically formed by constituting submodules with a self-similar relation as indicated by Eq. (2). These submodules have a large modularity as indicated by scaling analysis in Section VI.

A surprising consequence of Eqs. (1) and (2) is that the network at high  $p$ -values (i.e. determined by strong links) lacks the small-world logarithmic scaling  $\langle \ell \rangle \sim \log N_c$  [6] believed to be necessary for efficient information transfer in the network [5, 7]. Indeed, a fractal network [24] poses much larger distances than those appearing in small-worlds: a distance  $\ell_{\max} \sim 100$  observed in Fig. 2 would require an enormous small-world network of the order  $N_c \sim 10^{100}$ , rather than  $N_c \sim 10^4$  as observed for fractal networks. The structural differences between a modular fractal network and a small-world network are starkly revealed when we

rewire a typical percolation module achieved by randomly reconnecting links while keeping the degree of each node intact. The topology of the rewired module is depicted in the left panel of Fig. 2 which should be compared to the original module in the right panel. The rewired network has become small-world with the apparent loss of the modular structure. Indeed, the rewired networks have very small average distances  $\langle \ell \rangle \approx 3$  with the concomitant exponential behaviour,  $N_c = \exp \langle \ell \rangle / \ell_0$  with a very small characteristic size  $\ell_0 = 1/7$ , as shown in the central panel of Fig. 2. The crux of the matter is how functional modules in the brain can be connected closely without collapsing into a cohesive small-world structure.

**Short-cut wiring is optimal for efficient flow.**— When we extend the percolation analysis lowering further the threshold  $p$ , weaker ties are incorporated to the network connecting the self-similar modules through short-cuts. A typical scenario is depicted in Fig. 4A showing three percolation modules identified at the first jump in Fig. 1B at  $p = 0.98$ . At this tie strengths, the modules are separated and show submodular fractal structure indicated in the colored boxes. When we lower  $p = 0.975$ , Fig. 4B, modules are connected with each other and a global incipient component starts to appear linking the whole brain. A second global percolation-like transition appears in the system identified when the mass of the largest component occupies half of the activated area (Fig. 4C). For different individuals, global percolation occurs in the interval  $p_c = [0.945, 0.96]$  as indicated in the inset of Fig. 1A.

Our next aim is to characterize this two-layer network formed by an underlying fractal structure determined by strong links, shortcuted by weak ties. The spatial distribution of shortcuts (the weak links) will determine topological properties of the network. When the cumulative probability distribution to find a Euclidean distance between two connected nodes,  $r_{ij}$ , larger than  $r$  follows a power-law:

$$P(r_{ij} > r) \sim r^{-\alpha+1}, \quad (3)$$

statistical physics makes precise predictions about optimization schemes for global function of the network as a function of the relation between the shortcut exponent  $\alpha$  and the dimension of the network  $d_f$  [16, 27, 28]. Specifically, there are three critical values for  $\alpha$  as shown schematically in Fig. 4D. If  $\alpha$  is too large then shortcuts will not be sufficiently long and the network will behave as fractal, similarly to the underlying structure. Below a critical value determined by the relation  $\alpha < 2d_f$  [16], shortcuts are sufficient to convert the network in a

small world. Within this regime there are two significant optimization values:

(i) Wiring cost minimization with full routing information. This assumes a network of dimension  $d_f$ , over which short-cuts are added to optimize communication, with a wiring cost constraint proportional to the total shortcut length. It is also assumed that coordinates of the network are known, i.e. it is the shortest path that it is being minimized. Under these circumstances it is found that the optimal distribution of shortcuts corresponds to a power-law Eq. (3) with  $\alpha = d_f + 1$  [28]. This precise scaling is found in the US airport network [29] where a cost limitation applies to maximize profits.

(ii) Decentralized searches with only local information. This corresponds to the classic Milgram’s “small-world experiment” of decentralized search in social networks [27], where a person (a node) has knowledge of local links and of the final destination but not of the intermediate routes. Under these circumstances, which also apply to routing packets in the Internet, the problem corresponds to a greedy search, rather than to optimization of the minimal path. The optimal relation is obtained when  $\alpha = d_f$  [16, 27].

Hence, the analysis of the distribution of shortcuts provides information both on the topology of the resulting network and on which transport procedure is optimized. To investigate how short-cuts are distributed, we analyze the cumulative probability distribution of the Euclidean length between two nodes  $i, j$  connected by the weak ties. This distribution reveals a well defined power-law behavior Eq. (3) with an exponent  $\alpha = 3.1 \pm 0.1$  (see Fig. 4E). Given the value obtained in Eq. (1),  $d_f = 2.1$ , this implies that the network composed of strong and weak links is small-world ( $\alpha < 2d_f$ ) and optimizes wiring cost assuming full knowledge of routing information ( $\alpha = d_f + 1$ ).

The existence of modular organization of strong ties in a sea of weak ties is reminiscent of the structure found to bind dissimilar communities in social networks. Granovetter’s work on social networks [17, 18] proposes the existence of weak ties to coheses well-defined social groups into a large-scale social network. Such a two-scale structure has a large impact on the diffusion and influence of information across the entire social structure. Our observation of this two-layer organization in brain networks suggests that it may be a ubiquitous natural solution to the puzzle of information flow in highly modular structures.

Previous studies have found that wiring of neuronal networks at the cellular level is close to optimal [13, 30]. Specifically it is found that long-range connections do not minimize wiring but achieve network benefits. In agreement with this observation, at the mesoscopic

scale explored here, we find an optimization which reduces wiring cost while maintaining network proximity. An intriguing element of our observation is that this minimization assumes that broadcasting and routing information are known to each node. How this may be achieved— what aspects of the neural code convey its own routing information— remains an open question in neuroscience.

- 
- [1] S. Dehaene, L. Naccache, *The cognitive neuroscience of consciousness*, The MIT Press, 1-37, (2001).
- [2] D. J. Felleman, D. C. van Essen, *Cereb. Cortex* **1**, 1 (1991).
- [3] A. Treisman, *Current opinion in neurobiology* **6**, 171 (1996).
- [4] G. Tononi, O. Sporns, G. M. Edelman, *Proc. Nat. Acad. Sci. USA* **91**, 5033 (1994).
- [5] O. Sporns, D. R. Chialvo, M. Kaiser, C. C. Hilgetag, *Trends Cognit. Sci.* **8**, 418 (2004).
- [6] D. Watts, S. Strogatz, *Nature* **393**, 440 (1998).
- [7] D. S. Bassett, E. Bullmore, *Neuroscientist* **12**, 512 (2006).
- [8] S. Achard, R. Salvador, B. Whitcher, J. Suckling, E. Bullmore, *J. Neurosci.* **26**, 63 (2006).
- [9] S. Achard, E. Bullmore, *PLoS Comput. Biol.* **3**, e17 (2007).
- [10] V. M. Eguiluz, D. R. Chialvo, G. A. Cecchi, M. Baliki, A. V. Apkarian, *Phys. Rev. Lett.* **94**, 018102 (2005).
- [11] Y. He, Z. J. Chen, A. C. Evans, *Cereb. Cortex* **17**, 2407 (2007).
- [12] P. Hagmann, M. Kurant, X. Gigandet, P. Thiran, V. J. Wedeen, R. Meuli, J. P. Thiran, *PLoS One* **2**, e597 (2007).
- [13] S. Song, P. J. Sjoström, M. Reigl, S. Nelson, D. D. Chklovskii, *PLoS Biol.* **3**, e68 (2005).
- [14] S. Yu, D. Huang, W. Singer, D. Nikolic, *Cereb. Cortex* **18**, 2891 (2008).
- [15] C. J. Stam, B. F. Jones, G. Nolte, M. Breakspear, P. Scheltens, *Cereb. Cortex* **17**, 92 (2007).
- [16] H. D. Rozenfeld, C. Song, H. A. Makse, *Phys. Rev. Lett.* **104**, 025701 (2010).
- [17] M. S. Granovetter, *American Journal of Sociology* **78**, 1360 (1973).
- [18] J.-P. Onnela, J. Saramaki, J. Hyvonen, G. Szabo, D. Lazer, K. Kaski, J. Kertesz, A.-L. Barabasi, *Proc. Nat. Acad. Sci. USA* **104**, 7332 (2007).
- [19] G. Tononi, G. M. Edelman, *Science* **282**, 1846 (1998).
- [20] B. J. Baars, *In the theater of consciousness: The workspace of the mind* (Oxford University Press, USA, 1997).
- [21] H. Pashler, *Psychological Bulletin*, **116**, 220 (1994).
- [22] M. Sigman, S. Dehaene, *J. Neurosci.* **28**, 7585 (2008).
- [23] A. Bunde, S. Havlin, editors. *Fractals and Disordered Systems*, 2nd edition (Springer-Verlag, Heidelberg, 1996).

- [24] C. Song, S. Havlin, H. A. Makse, *Nature* **433**, 392 (2005).
- [25] F. Radicchi, J. J. Ramasco, A. Barrat, S. Fortunato, *Phys. Rev. Lett.* **101**, 148701 (2008).
- [26] C. Song, L. K. Gallos, S. Havlin, H. A. Makse, *J. Stat. Mech.*, P03006 (2007).
- [27] J. Kleinberg, *Nature* **406**, 845 (2000).
- [28] G. Li, S. D. S. Reis, A. A. Moreira, S. Havlin, H. E. Stanley, J. S. & Andrade Jr, *Phys. Rev. Lett.* **104**, 018701 (2010).
- [29] G. Bianconi, P. Pin, M. Marsili, *Proc. Nat. Acad. Sci. USA* **106**, 11433 (2009).
- [30] M. Kaiser, C. C. Hilgetag, *PLoS Comput. Biol.* **2**, e95 (2006).

FIG. 1. **Percolation Analysis.** (A) Size of the largest connected component of nodes (as measure by the fraction to the total system size) as a function of percolation threshold  $p$ . The main plot shows the size of the largest connected component for every one of the 16 subjects for a given set of the 4 conditions. The curves follow the general percolation shape rising rapidly to 1 in a narrow range of  $p$  around 0.95, albeit with discrete jumps. The inset presents a detail around  $p \approx 0.95$ . (B) This panel shows a detail for a single individual. As we lower  $p$  the size of the largest component increases in jumps when new modules emerge, grow, and finally get absorbed by the largest component. We follow and plot the evolution of the modules by plotting components with more than 1,000 voxels for a given  $p$  value. The right lower panel shows a typical module in network representation. The same module is shown embedded in real space in the left lower panel - this specific module projects to the medial occipital cortex, see Section V for the spatial projection of all modules.

FIG. 2. **Strong ties define fractal modules.** The central panel shows the number of voxels or mass of each module,  $N_c$ , as a function of different length scales in network and real space. Each point represents a bin average over the modules for all individuals and conditions. In this plot we use all the modules appearing at the first jump in Fig. 1A. The mass of the modules is plotted as a function of the maximum network diameter,  $\ell_{\max}$ , the average network path,  $\langle \ell \rangle$ , and the Euclidean diameter of a module,  $r_{\max}$ . The last one yields the Hausdorff fractal dimension,  $d_f$ , Eq. (1). A typical percolation module in network representation is shown in the right panel. The colors identify scale invariant sub-modules in the network as found by the box-covering algorithm explained in Section IV. The network has a very rich modular structure typical of fractal topologies [24]. The fractal module contains 4097 nodes. The large diameter of this network is visually apparent, with an average chemical distance  $\langle \ell \rangle = 41.7$ , large chemical diameter  $\ell_{\max} = 139$ , and Euclidean diameter  $r_{\max} = 136$  mm. When the links of the network of each module are randomly rewired, preserving the degree of each node, we find an exponential behavior  $N_c = \exp [7\langle \ell \rangle]$  characteristic of small-world networks [6] as shown in the central panel. The left panel shows the topology of the rewired network where the modular structure disappears and the network becomes a typical small-world structure characterized by very short average distance between nodes.

FIG. 3. **Fractal submodules in network space.** (A) Detection of submodules and fractal dimension inside the modules. We demonstrate the box-covering algorithm for a

schematic network, following the Maximum Excluded Mass Burning algorithm in [24, 26] (see Section IV). We cover a network with boxes of size  $\ell_B$  which are identified as sub-modules to reveal the self-similar structure. **(B)** Scaling of the number of boxes  $N_B$  needed to cover the network of a module as a function of length of the boxes  $\ell_B$  (measured in topology space), yielding the network fractal dimension  $d_B$ .

FIG. 4. **Weak ties are optimally distributed.** **(A)** Three modules identified at the first jump for the subject shown in Fig. 1B for  $p = 0.98$ . **(B)** When we lower the threshold to  $p = 0.975$ , weak ties connect the modules. Blue lines represent the weak links with distance longer than 10 mm and the light blue nodes are the nodes added from **A**. **(C)** Real space representation of the modules connected by weak ties (blue lines) as the network achieves the second global percolation where the largest component is half the total mass. **(D)** Sketch of the different critical values of the shortcut exponent  $\alpha$  in comparison with  $d_f$ . **(E)** Cumulative probability distribution  $P(r_{ij} > r)$  of Euclidean distances  $r_{ij}$  between any two voxels that are directly connected in the correlation network. The straight line fitting yields a exponent  $\alpha - 1 = 2.1 \pm 0.1$  indicating optimal information transfer with wiring cost minimization [28].

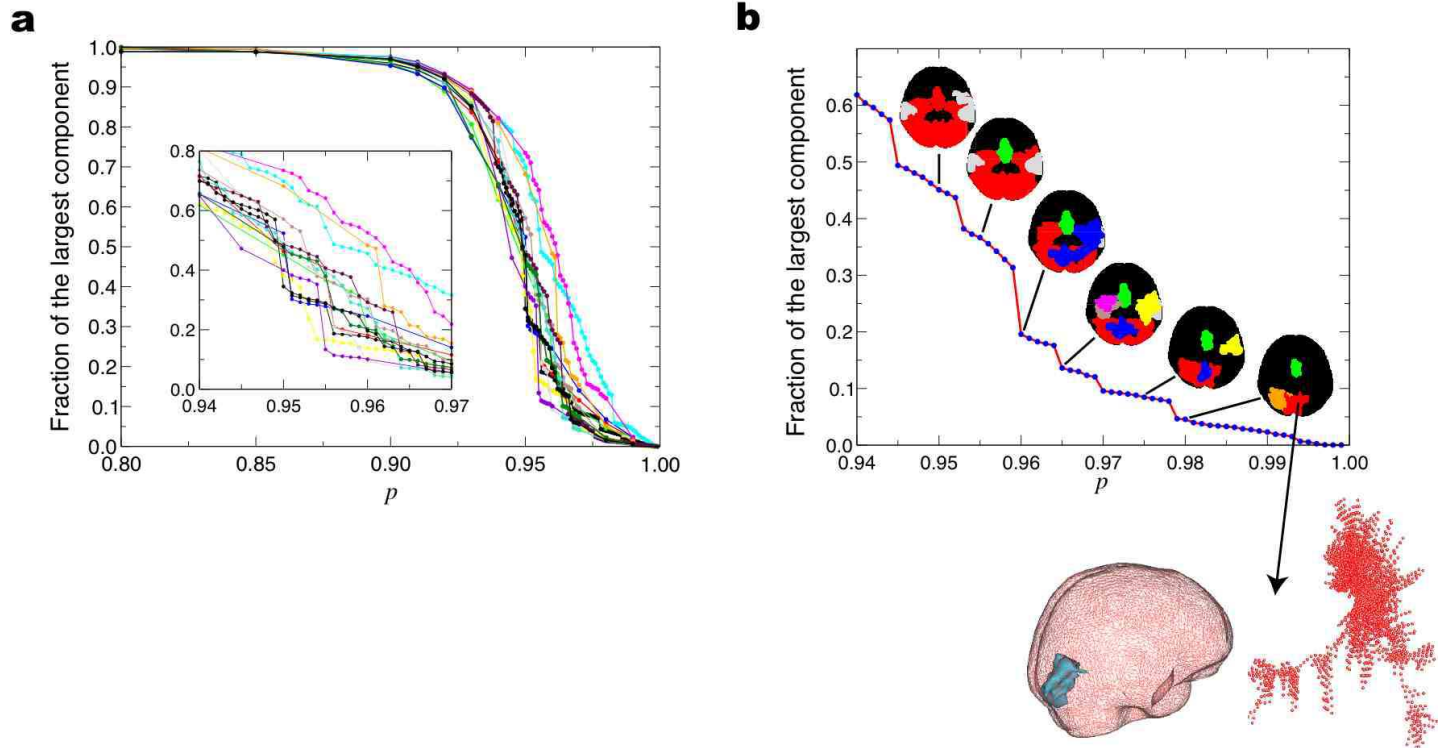


FIG. 1:

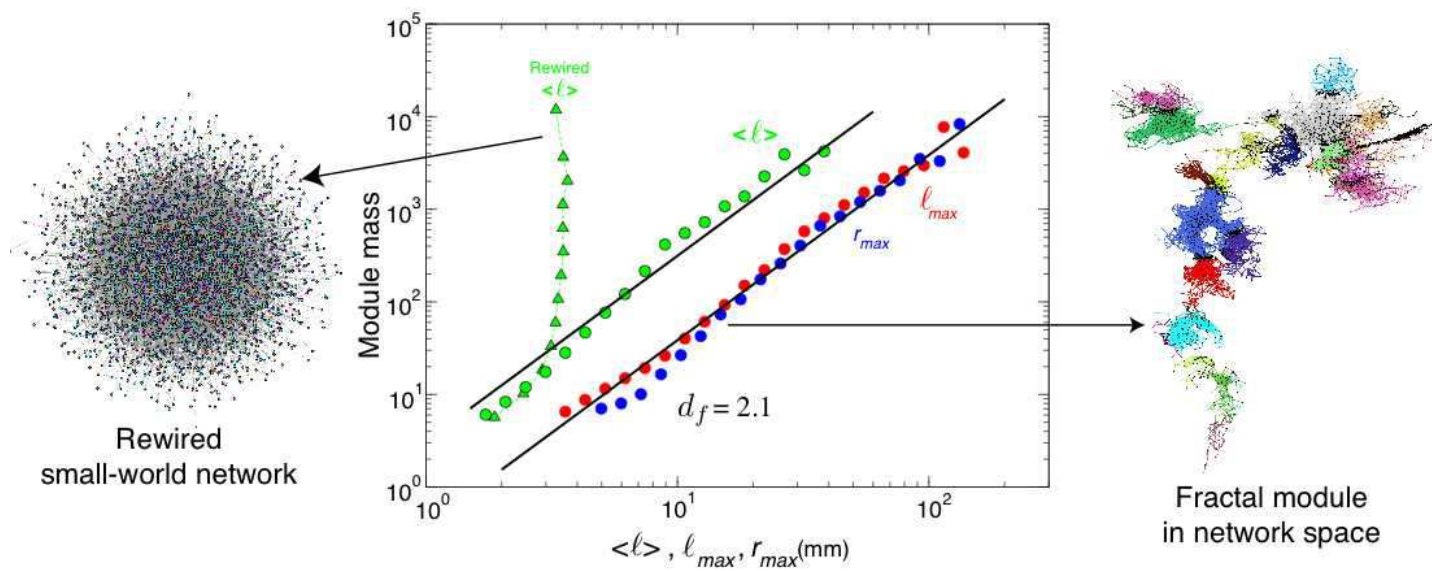


FIG. 2:

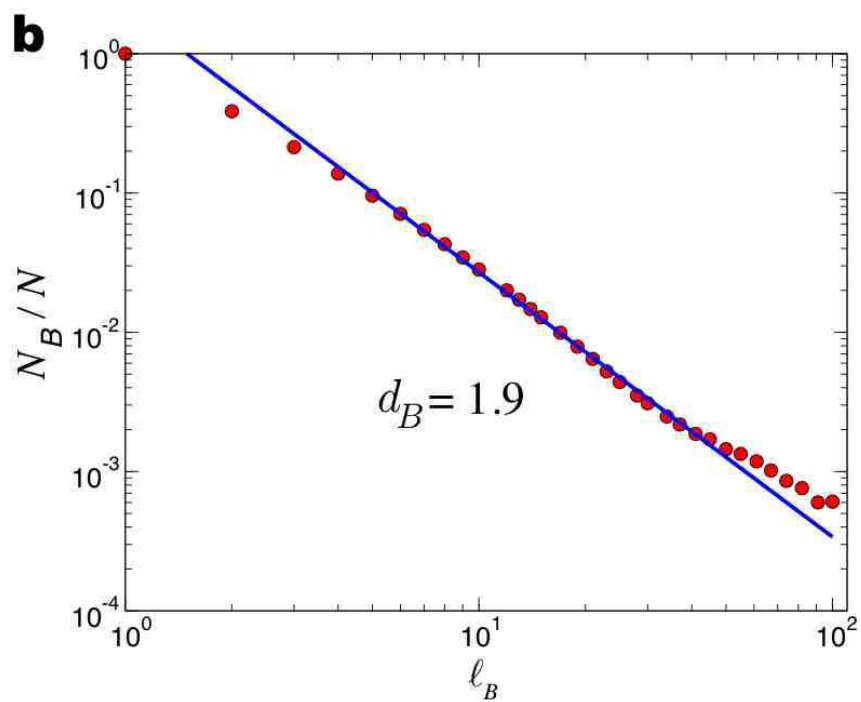
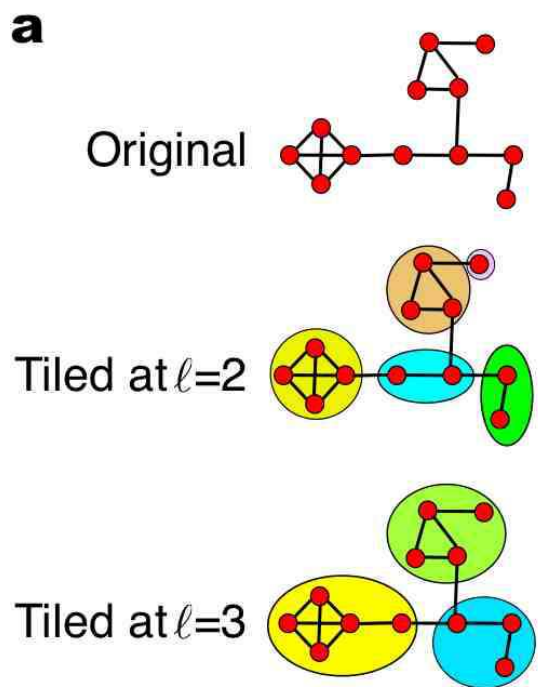


FIG. 3:

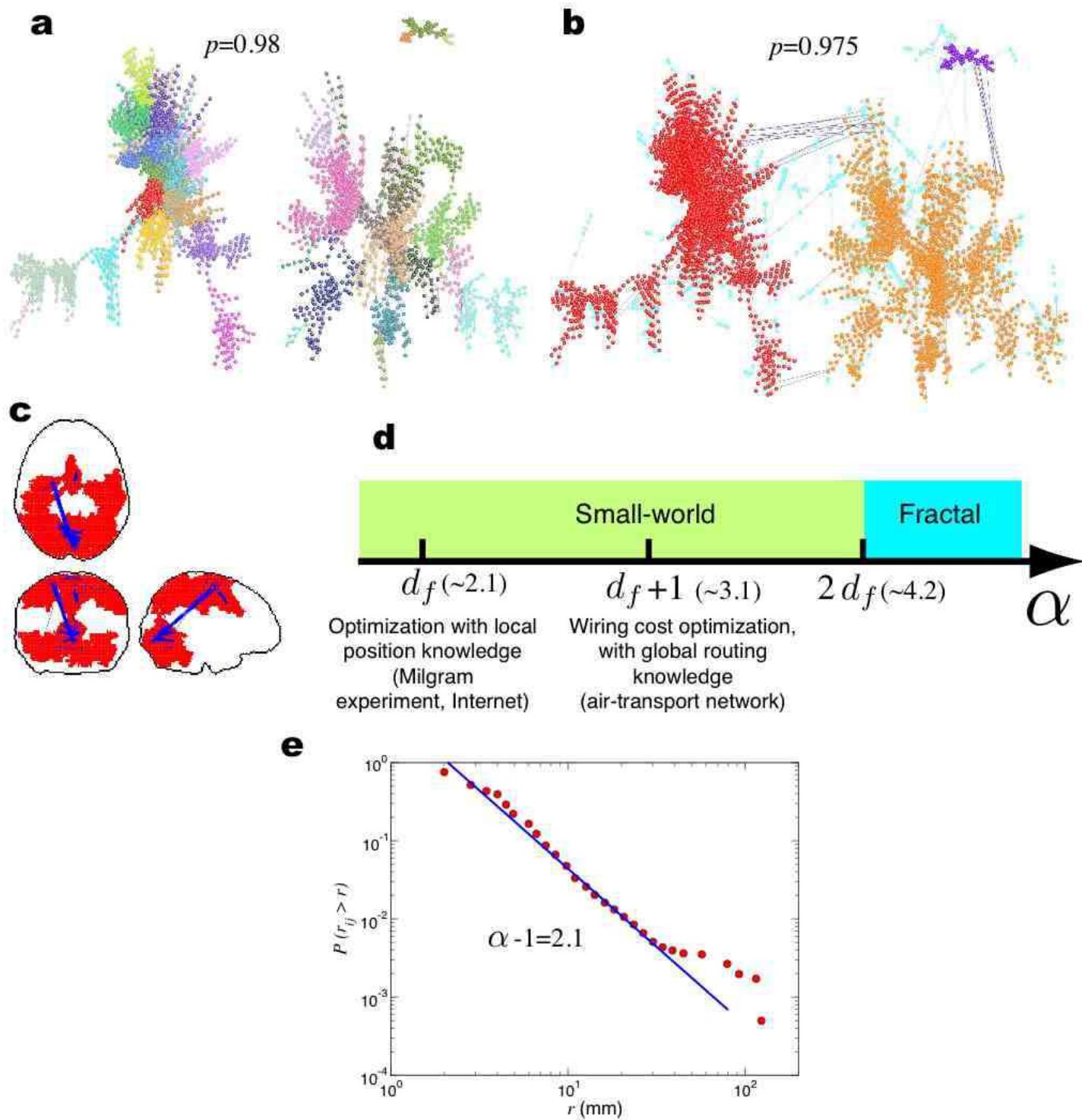


FIG. 4:

## APPENDIX

### I. EXPERIMENTAL DESIGN: FMRI STUDIES

Participants performed a dual-task paradigm: first a visual task of comparing an Arabic numeral (target T1) to a fixed reference, with a right-hand response and, second, an auditory task of judging the pitch of an auditory tone (target T2) with a left-hand response. The stimulus onset asynchrony (SOA) between T1 and T2 was varied between 0, 300, 900 and 1,200 ms. For the purpose of this experiment we only analyze the simultaneous presentation, i.e. the SOA = 0 condition.

While subjects performed the dual-task, we recorded whole-brain fMRI images at a sampling time (TR) of 1.5 s, and computed the phase and amplitude of the hemodynamic response. This ‘activated or functional map’ exhibits phases consistently falling within the expected response latency for a task-induced activation. As expected for an experiment involving visual and auditory stimuli and bi-manual responses, the responsive regions included bilateral visual occipito-temporal cortices, bilateral auditory cortices, motor, premotor and cerebellar cortices, and a large-scale bilateral parieto-frontal structure [22]. We performed an analysis of the phase signal [22] which can yield a temporal resolution for whole-brain imaging of about  $\sim 100$ -200 ms, well beyond the typical resolution of fMRI, which is in the range of  $\sim 1$ s.

### II. PHASE CORRELATIONS AND FUNCTIONAL BRAIN NETWORK

We use network theory concepts for the analysis of correlations between different brain areas, based on the temporal activation of voxels when a subject responds to an external stimulus. We reconstruct the network topology of brain voxels, where a network link indicates a high correlation in the phase-space activity of the two connected voxels, and compare this structure with the corresponding topology of the voxel location in the brain.

For each participant and each stimulus we have recorded the time evolution of the phase over 440 s for all brain voxels,  $a_i(t)$ . Thus, we have a total of 64 measurements, as resulting from the 4 different stimuli presented to the 16 subjects. For our analysis, we create a mask where we only keep voxels which were activated in more than 75% of the cases, i.e. in at

least 48 instances.

We consider the phase difference  $a_i(t) - a_j(t)$  as a function of time between any two voxels  $i$  and  $j$  in the activated mask, averaged over  $T = 40$  snapshots for each subject/stimulus. The number of activated voxels is around  $N \approx 60,000$ , slightly varying for different individuals. The correlation  $c_{ij}$  between two voxels is given by

$$c_{ij} = \frac{1}{T} \sum_{t=1}^T \cos(a_i(t) - a_j(t)). \quad (4)$$

We link two voxels if their correlation  $c_{ij}$  is larger than a threshold value  $p$ . The resulting network is a representation of functional relations among voxels for a specific subject and stimulus.

### III. PERCOLATION

We use percolation theory [23] to identify the functional modules resulting from the correlation between the phases of two voxels. The topology of this network strongly depends on the value of  $p$ . The variation of  $p$  describes a percolation process. A large  $p$  value enables isolated module identification, since only the strongest (i.e. more correlated) functional links between voxels are preserved. As  $p$  is lowered, these modules get progressively merged to larger entities and the emphasis is shifted towards large-scale properties of the spanning network. Figure 1B lower right panel shows a sample module in network space.

The complex network representation reveals functional links between brain areas, but cannot directly reveal spatial correlations. Since voxels are embedded in space, we also study the topological features of modules in three dimensions, where now voxels assume their known positions in the brain and links between them are transferred from the corresponding network, i.e. they are assigned according to the degree of correlation between any two voxels, independently of the voxels proximity in real space. The above procedure yields a different network or spatial module for each subject; an example is shown in Fig. 1B lower left panel. We study each of these networks separately and show that they all carry statistically similar properties.

#### IV. BOX COVERING ALGORITHM FOR FRACTAL DIMENSION IN NETWORK SPACE

For a given percolation module, the detection of submodules or boxes follows from the application of the box-covering algorithm for self-similar networks [24, 26]. The algorithm can be downloaded at [http://lev.ccny.cuny.edu/~hmakse/soft\\_data.html](http://lev.ccny.cuny.edu/~hmakse/soft_data.html). In box covering we assign every node to a box or submodule, by finding the minimum possible number of boxes,  $N_B(\ell_B)$ , that cover the network and whose diameter (defined as the maximum distance between any two nodes in this box) is smaller than  $\ell_B$ . These boxes are characterized by the proximity between all their nodes, at a given length scale. Different values of the box diameter  $\ell_B$  yield boxes of different size. These boxes are identified as submodules which merge into larger entities as we increase  $\ell_B$ .

We implement the Maximum Excluded Mass Burning (MEMB) algorithm from [26] for box covering. The algorithm uses the basic idea of box optimization, where we require that each box should cover the maximum possible number of nodes, and works as follows: For a given  $\ell_B$ , we first locate the optimal ‘central’ nodes which will act as the origins for the boxes. This is done by first calculating the number of nodes (called the mass) within a diameter  $\ell_B$  from each node. The node that yields the largest mass is marked as a center. Then we mark all the nodes in the box of this center node as ‘tagged’. We repeat the process of calculating the mass of the boxes starting from all non-center nodes, and we identify a second center according to the largest remaining mass, while nodes in the corresponding box are ‘tagged’, and so on. When all nodes are either centers or ‘tagged’ we have identified the minimum number of centers that can cover the network at the given  $\ell_B$  value. Starting from these centers as box origins, we then simultaneously burn the boxes from each origin until the entire network is covered, i.e. each node is assigned to one box (we call this process burning since it is similar to burning algorithms developed to investigate clustering statistics in percolation theory [23]). In Fig. 3A of the main text we show how box-covering works for a simple network at different  $\ell_B$  values.

## V. SPATIAL PROJECTION

Percolation modules were purely determined based on their network properties. We investigate whether they map consistently, for different subjects, to specific brain regions. Since the  $p$ -values at which each module appears varies across subjects, we first determine, for each subject, the highest correlation  $p$ -value for which there are at least four modules.

The topography of these modules reflects coherent patterns across different subjects. In virtually all subjects we observe a module covering the anterior cingulate (AC) region, a module covering the medial part of the posterior parietal cortex (PPC) and a module covering the medial part of posterior occipital cortex (area V1/V2), along the calcarine fissure (see Fig. 5 for a medial sagittal view of the first four percolation modules for all the participants in a typical stimulus).

We measure the likelihood that a voxel may appear in a percolation module by counting, for each voxel, the number of individuals for which it was included in one of the first four percolation modules (Fig. 6A). The spatial distribution of the first percolation modules averaged over all the subjects shown in Fig. 6B and 6c shows that modules in the three main nodes, V1/V2, AC and PPC, are ubiquitously present in percolation modules and, to a lesser extent, voxels in the motor cortex (along the central sulcus) slightly more predominantly on the left hemisphere. Thus, the correlation networks obtained from each subject yield modules with consistent topographic projections.

## VI. QUANTIFYING THE MODULARITY OF THE BRAIN MODULES

The MEMB algorithm for box covering is driven by the proximity between nodes and the maximization of the mass associated with each box center [24, 26]. In the case of MEMB we have the additional benefit of detecting submodules at different scales, so that we can study the hierarchical character of modularity, i.e. modules of modules, and we can detect whether modularity is a feature of the network that remains scale-invariant.

Thus, the box-covering concept acts as a community detection algorithm that identifies submodules of size  $\ell_B$  composed of highly connected brain areas. The requirement of minimal number of boxes to cover the network ( $N_B$ ) guarantees that the partition of the network is such that each submodule contains the largest possible number of nodes and links inside the

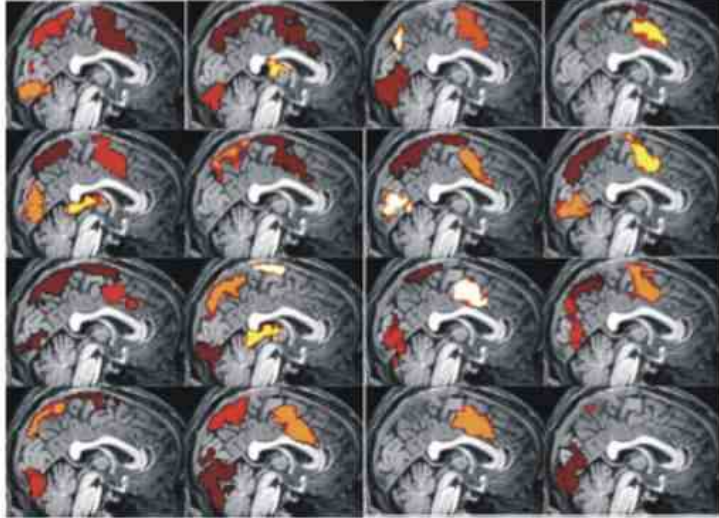


FIG. 5: **The emerging modules have consistent spatial projections.** The plot shows the spatial distribution of the four largest percolation modules. Each image corresponds to a different subject. Most modules are localized in the same regions: anterior cingulate, posterior medial-occipital, posterior parietal and thalamus. The anterior cingulate, a fundamental node in cognitive control is the only shared region for all subjects.

submodule with the constraint that the submodules cannot exceed size  $\ell_B$ . This optimized tiling process gives rise to submodules with the fewest number of links connecting to other submodules implying that the degree of modularity, defined by [1–4]:

$$\mathcal{Q}(\ell_B) \equiv \frac{1}{N_B} \sum_{i=1}^{N_B} \frac{L_i^{\text{in}}}{L_i^{\text{out}}}, \quad (5)$$

is maximized. Here  $L_i^{\text{in}}$  and  $L_i^{\text{out}}$  represent the number of links that start in a given submodule  $i$  and end either within or outside  $i$ , respectively. Large values of  $\mathcal{Q}$  (i.e.  $L_i^{\text{out}} \rightarrow 0$ ) correspond to a higher degree of modularity [3].

The value of the modularity of the network  $\mathcal{Q}$  varies with  $\ell_B$ , so that we can detect the dependence of modularity on different length scales, or equivalently how the modules themselves are organized into larger modules that enhance the degree of modularity.

Analysis of the modularity Eq. (5) in Fig. 7 reveals a monotonic increase of  $\mathcal{Q}(\ell_B)$  with a lack of a characteristic value of  $\ell_B$ . Indeed, the data can be approximately fitted with a power-law functional form:

$$\mathcal{Q}(\ell_B) \sim \ell_B^{d_M}, \quad (6)$$

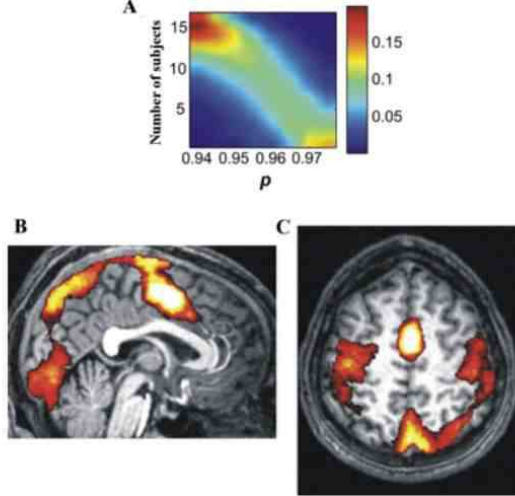


FIG. 6: **Spatial structure of the modules.** **a**, This panel denotes the fraction of the total number of voxels that appear to one of the four largest modules in  $n$  subjects at a given percolation threshold  $p$ . As we reduce the threshold the peak shifts towards larger  $n$  values, i.e. the same voxels appear consistently in the largest modules for all subjects. **b**, and **c**, These panels show the spatial distribution of the first percolation module (in subject counts). The two brain slices show for the highest  $p$ -values the shared voxels. White bleached regions correspond to voxels which are included in the first percolation module for all subjects. Most modules are localized to the same regions: anterior cingulate, posterior medial-occipital, posterior parietal and thalamus.

which is detected through the modularity exponent  $d_M$ . We characterize the network using different subjects and we find that  $d_M \approx 1.6$  is approximately constant over different individuals (Fig. 7).

This value reveals a considerable degree of modularity in the entire system as evidenced by the network structure shown in the right panel of Fig. 2. For comparison, a random small-world network with no modularity (left panel Fig. 2) has  $d_M = 0$  and a high modular structure has  $d_M = d_B$  [3]. The lack of a characteristic length-scale in the modularity shown in Fig. 7 suggests that the modules appear at all length-scales, i.e. submodules are organized within larger modules in a self-similar way, so that the inter-connections between those modules repeat the basic modular character of the entire brain network. Thus, the modular organization of the network remains statistically invariant when observed at different scales.

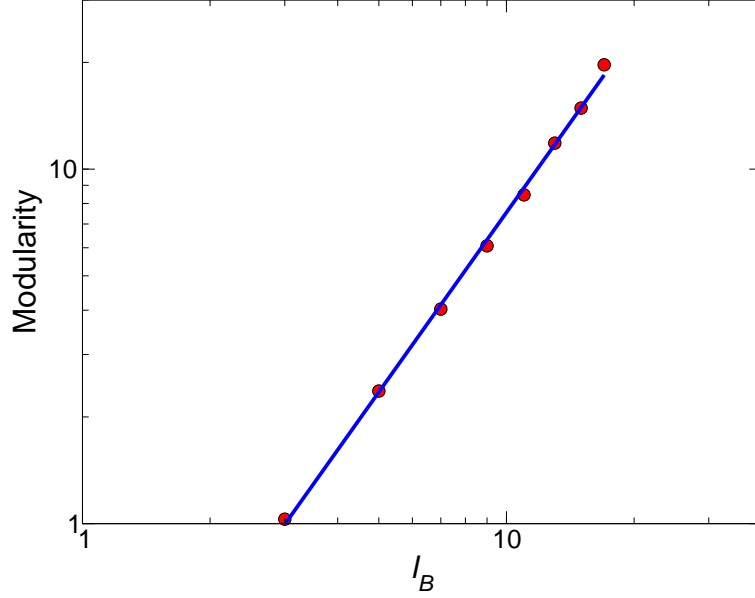


FIG. 7: **Quantifying the modularity of the brain modules.** The identified brain modules are highly modular, as can be seen by the scaling of  $Q(\ell_B)$  with  $\ell_B$  that yields a modularity exponent around  $d_M = 1.6$ .

- [1] M. E. J. Newman, M. Girvan, *Phys. Rev. E* **69**, 026113 (2004).
- [2] G. Caldarelli, A. Vespignani, (eds). *Large scale structure and dynamics of complex networks*. (World Scientific, Singapore, 2007).
- [3] L. K. Gallos, C. Song, S. Havlin, H. A. Makse, *Proc. Nat. Acad. Sci. USA* **104**, 7746 (2007).
- [4] V. Galvao, J. G. V. Miranda, R. F. S. Andrade, J. S. Andrade Jr., L. K. Gallos, H. A. Makse, *Proc. Nat. Acad. Sci. USA* **107**, 5750 (2010).